

Type-II multiferroic $\text{Hf}_2\text{VC}_2\text{F}_2$ MXene monolayer with high transition temperature

Jun-Jie Zhang,^{†,‡} Linfang Lin,[†] Yang Zhang,[†] Menghao Wu,[¶] Boris I.
Yakobson,^{*,‡} and Shuai Dong^{*,†}

[†]*School of Physics, Southeast University, Nanjing 211189, China*

[‡]*Department of Materials Science and NanoEngineering, Rice University, Houston, Texas
77005, United States*

[¶]*School of Physics and Wuhan National High Magnetic Field Center, Huazhong University
of Science and Technology, Wuhan 430074, China*

E-mail: biy@rice.edu; sdong@seu.edu.cn

Abstract

Achieving multiferroic two-dimensional (2D) materials should enable numerous functionalities in nanoscale devices. Until now, however, predicted 2D multiferroics are very few and with coexisting yet only loosely coupled (type-I) ferroelectricity and magnetism. Here, a type-II multiferroic MXene $\text{Hf}_2\text{VC}_2\text{F}_2$ monolayer is identified, where ferroelectricity originates directly from its magnetism. The noncollinear Y-type spin order generates a polarization perpendicular to the spin helical plane. Remarkably, the multiferroic transition is estimated to occur above room temperature. Our investigation should open the door to a new branch of 2D materials for pursuit of intrinsically strong magnetoelectricity.

Keywords

MXenes, ferroelectrics, multiferroics

Two-dimensional (2D) materials have attracted attention since the experimental discovery of graphene.¹ Divers properties and functions are discovered in plentiful 2D materials, going beyond the original appeal as new semiconductors. More and more important physical properties existing in three-dimensional (3D) crystals have also been found to appear in the 2D form. For example, 2D superconductivity,²⁻⁶ 2D ferromagnetism,⁷⁻⁹ as well as 2D ferroelectricity,¹⁰⁻²¹ have recently been confirmed in experiments or predicted via calculations.

Ferromagnetism and ferroelectricity, with switchable ferro-vectors, play crucial roles in various devices. Thus, their existence in 2D materials would be very attractive. On one hand, since the first prediction of 2D ferroelectric (FE) hydroxylized graphene in 2013,¹⁰ more 2D materials, e.g. 1T-MoS₂, In₂Se₃, 2D materials functionalized with polar groups, etc., have been predicted to be FE.¹¹⁻¹⁹ Experimentally, in-plane FE polarization (P) was observed and manipulated in atom-thick SnTe,²⁰ while out-of-plane FE P was found in few layers CuInP₂S₆.²¹ The involved mechanisms are either polar phonon modes or polar functional groups. On the other hand, many 2D ferromagnets have been predicted,^{8,9} and recently CrI₃ monolayer is experimentally confirmed.⁷

The coexisting magnetism and polarization lead to the multiferroicity.^{22,23} The coupling between these two ferro-vectors allows the control of charge via magnetic field or the control of spin via electric field. In fact, a few 2D multiferroics were also recently predicted,^{16,19,24,25} in which the origins of polarization and magnetism are independent of each other (i.e. they are all type-I multiferroics²⁶). Thus their magnetoelectric coupling is indirect and weak.

To pursue the intrinsically strong magnetoelectricity, a possible route is to design 2D type-II multiferroics (i.e. magnetic ferroelectrics²⁶), in which the FE P is directly generated and thus fully controlled by magnetic order.^{22,23} Although the type-II multiferroics have been extensively studied, these materials have not gone into the zone of 2D materials. Even some type-II multiferroics own layered structures, e.g. CuFeO₂,²⁷ Sr₃NiTa₂O₉,²⁸ and

Ba₃MnNb₂O₉,²⁹ the inter-layer couplings are via ionic bonds, difficult to be exfoliated.

In this work, monolayer carbides and carbonitrides, i.e. MXenes ($M_{n+1}X_nT_x$, M : early transition metal; X : carbon or nitrogen), are predicted as 2D type-II multiferroics. As a new branch of 2D materials, MXenes have been experimentally produced by selectively etching the A-layers from their 3D parent compounds MAX.³⁰⁻³² The surface can be easily covered by functional groups (e.g. $T=F$, O, or/and OH), resulting in diversiform chemical and physical properties.^{5,33} Recently, an ordered double transition metal MAX with Cr-Al/Mo-Al bonding were synthesized, e.g. Cr₂TiAlC₂³⁴ and Mo₂TiAlC₂,³⁵ in which a Ti-layer is sandwiched between two outer Cr/Mo carbide layers in the M_3AX_2 structure. Then ordered double transition metal carbides M'_2MX_2 and $M'_2M_2X_3$, e.g. Mo₂TiC₂T_x, Mo₂Ti₂C₂T_x and Cr₂TiC₂T_x, were successfully realized by etching the Al-layers.³⁶ In addition, considering the transition metals involved, many MXenes should be intrinsically magnetic (at least from the theoretical viewpoint), and their magnetism depends on M (M') and T .^{8,9} For instance, Cr₂TiC₂F₂ and Cr₂TiC₂(OH)₂ are predicted to be antiferromagnetic (AFM), whereas Cr₂VC₂(OH)₂, Cr₂VC₂F₂, and Cr₂VC₂O₂ are ferromagnetic (FM).⁹ Herein, derived from experimental Hf₃C₂T_x monolayer,³⁷ the ordered double transition metal carbides Hf₂MC₂T₂ monolayers (possibly realized via 3D parent Hf₂MAIC₂)³⁸ are considered to be a 2D type-II multiferroics. Although both M and M' can be magnetic ions, here only the middle M layer is considered to be magnetic.

Candidate 2D MXene. According to the knowledge of type-II multiferroicity, some special frustrated magnetic orders, like noncollinear spiral magnetism or $\uparrow\uparrow\downarrow\downarrow$ -type AFM order, may break the space inversion symmetry and thus lead to FE P .^{22,23} The in-plane geometry of M ions is triangular, which is inherently frustrated if the nearest-neighbor (NN) exchange is AFM.^{27,28,39,40} Thus, to find MXenes with NN AFM interaction is the first step. According to the Goodenough-Kanamori rule,^{41,42} the ions with half-filled d shell usually lead to strong AFM exchanges. Besides, the half-filled Hubbard bands can lead to insulating, as required for ferroelectricity.

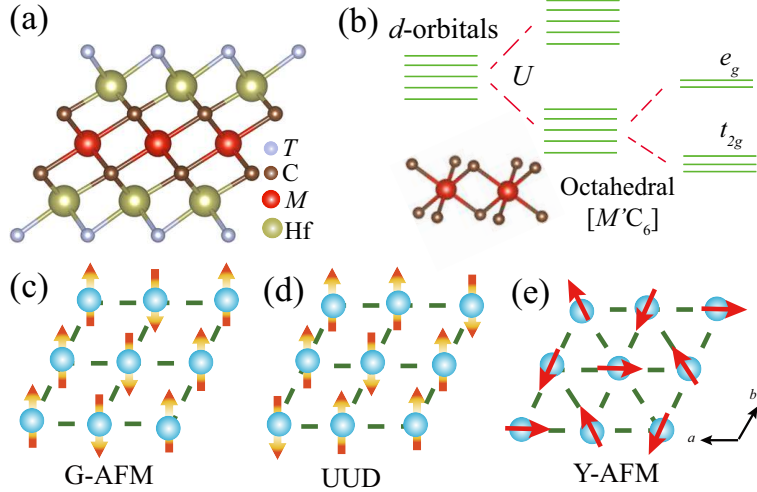


Figure 1: (a) Side views of the AA CG for $\text{Hf}_2\text{MC}_2\text{T}_2$. (b) Sketch of the energy splitting of $3d$ orbitals for M . (c-e) Sketch of possible AFM and ferrimagnetic spin orders in the 2D triangular lattice.

In $M'_2\text{MC}_2\text{T}_2$ MXene monolayer, each MC_6 forms an octahedron [1(a)]. The crystalline field of octahedron splits M 's d orbitals into the low-lying t_{2g} triplets and the higher-energy e_g doublets [1(b)]. To pursuit the half-filled Hubbard bands, high spin V^{2+} ($3d^3$), Nb^{2+} ($4d^3$), Mn^{4+} ($3d^3$), Mn^{2+} ($3d^5$), and Fe^{3+} ($3d^5$) are possible candidates to play as M .

To satisfy aforementioned conditions, in the following, $\text{Hf}_2\text{VC}_2\text{F}_2$, $\text{Hf}_2\text{NbC}_2\text{F}_2$, $\text{Hf}_2\text{MnC}_2\text{F}_2$, and $\text{Hf}_2\text{MnC}_2\text{O}_2$ will be calculated using density functional theory (DFT). Since Fe^{3+} ($3d^5$) can not be obtained if symmetric T layers are used, it is not considered here. In addition, $T=\text{OH}$ will be not calculated, considering its equal valence (and thus similar physical effects) to F.

DFT results. DFT calculations are performed to verify the multiferroicity of these MXene monolayers. Our calculations find that $\text{Hf}_2\text{VC}_2\text{F}_2$ is the most possible 2D type-II multiferroic material, while others are unlike due to various reasons (see Supplemental Materials for more details of DFT methods and results³⁸). The possibility of synthesis for $\text{Hf}_2\text{VC}_2\text{F}_2$ is also explored, which maybe realized via 3D parent Hf_2VAIC_2 . Based on experimentally produced V_3AlC_2 ³² and Hf_3AlC_2 ,⁴³ the hybrid energy for Hf_2VAIC_2 is about -90 meV/cell, implying such mix is more favorable. In addition, the possibility of MAX phase to MXenes

for Hf_2VAIC_2 are also verified by the crystal orbital Hamilton population (COHP) and exfoliation energies calculations.³⁸ Based on the results of COHP, the obtained bond strength between Hf and Al is very weaker than other bond between Hf/V and C in Hf_2VAIC_2 , which is similar to that in Hf_3AlC_2 and V_3AlC_2 , indicating the iconicity/metallicity characteristic between them. To further examine the progress of exfoliation, exfoliation energies are calculated as $E_{\text{exfoliation}} = -[E_{\text{tot}}(\text{MAX phase}) - 2E_{\text{tot}}(\text{MXene}) - E_{\text{tot}}(\text{Al})]/(4S)$,⁴⁴ where $E_{\text{tot}}(\text{MAX phase})$, $E_{\text{tot}}(\text{MXene})$ and $E_{\text{tot}}(\text{Al})$ stand for the total energies of bulk MAX phase, 2D MXene, and most stable bulk Al structure (Fm-3m), respectively. $S = \sqrt{3}a^2/2$ is the surface area and a is the lattice parameter of the MAX phase. Due to V_3AlC_2 was experimentally exfoliated into 2D Mxenes,³² Hf_2VAIC_2 which owns lower exfoliation energies have a better possibility to be exfoliated into MXenes. In summary, we conclude Hf_2VAIC_2 is a good candidate of 3D parent phase for the successful exfoliation into 2D Hf_2VC_2 MXenes. More details can be found in Supplemental Materials.³⁸

First, various configurations (CG's) for $\text{Hf}_2\text{VC}_2\text{F}_2$ are verified. Based on energy comparison and dynamic stability, the AA CG is confirmed to be the most favorable one,³⁸ where F ions stand just above/below the V's positions [1(a)]. Thus, our following investigation will focus on the AA CG only.

The nominal valences for Hf, V, C, and F are +4, +2, -4, and -1, respectively. Then for both C and F, the $2p$ -orbitals are fully occupied, while for Hf the $5d$ orbitals are fully empty. In this sense, the magnetism can only come from V, whose $3d$ orbitals own three electrons, as confirmed in the DFT calculation.

The magnetic ground state of $\text{Hf}_2\text{VC}_2\text{F}_2$ is searched by comparing the energies of various possible magnetic orders, including the nonmagnetic (NM), collinear FM, UUD type ferrimagnetic (stands for the "up-up-down" ferrimagnetic spin order), stripe AFM (G-AFM), as well as the 120° noncollinear AFM order (coined as Y-AFM here), as sketched in 1(c-e).

Considering the Hubbard-type correlations and spin-orbit coupling (SOC) for $3d$ and $5d$ orbitals, here a wide parameter space of $U_{\text{eff}}(\text{V})$ and $U_{\text{eff}}(\text{Hf})$ are scanned, as shown in 2(a)

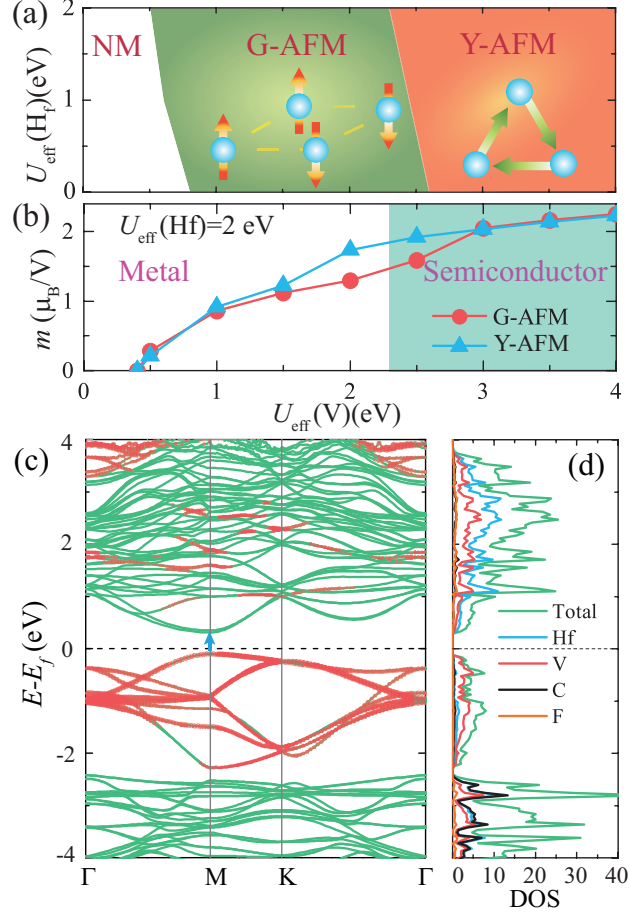


Figure 2: DFT results of $\text{Hf}_2\text{VC}_2\text{F}_2$ as a function of $U_{\text{eff}}(\text{Hf})$ and $U_{\text{eff}}(\text{V})$. (a) The ground state phase diagrams. (b) Local magnetic moment of V for G- and Y-AFM calculated within the default Wigner-Seitz sphere. Metallic and insulating regions are distinguished by colors. (c) The electronic band structure for Y-AFM with SOC calculated at $U_{\text{eff}}(\text{V}) = 3$ eV and $U_{\text{eff}}(\text{Hf}) = 2$ eV. The fat bands (red circles) are contributed (more than 50%) by 3d orbitals of V ions. (d) The corresponding density of states (DOS) and atom-projected DOS (PDOS).

and Supplemental Materials.³⁸ As expected, the $U_{\text{eff}}(\text{Hf})$ and SOC only have tiny effects on the magnetism due to Hf's empty $5d$ orbitals.³⁸ In contrast, with increasing $U_{\text{eff}}(\text{V})$, the magnetic ground-state undergoes two transitions, from NM to G-AFM first, then finally to Y-AFM. The local magnetic moment of V also depends on $U_{\text{eff}}(\text{V})$, increasing from 0 to more than $2 \mu_{\text{B}}/\text{V}$ (2(b)). Accompanying the second magnetic transition, the metal-insulator transition also occurs when $U_{\text{eff}}(\text{V}) > 2 \text{ eV}$.

Table 1: The calculated energies (E) of different magnetic structures using the HSE06 functional with SOC. The energy of FM is set as the reference. The corresponding local magnetic moments (m) are also listed.

	NM	FM	G-AFM	UUD	Y-AFM
E (eV/V)	0.09	0	-0.12	-0.14	-0.19
m (μ_{B}/V)		1.18	2.05	1.99	2.04

Due to the lack of experimental result on $\text{Hf}_2\text{VC}_2\text{F}_2$ monolayer, the HSE06 functional with SOC, are adopted as the benchmark to provide an alternative description.⁴⁵ As shown in 1, the HSE06 plus SOC calculation predicts that the Y-AFM is the ground state for $\text{Hf}_2\text{VC}_2\text{F}_2$ monolayer, and the corresponding magnetic moment is in good agreement with the result of $U_{\text{eff}}(\text{V}) = 3 \text{ eV}$ and $U_{\text{eff}}(\text{Hf}) = 2 \text{ eV}$, implying this set of parameters is proper. In fact, the same U_{eff} parameters were also adopted in previous studies,⁸ where only FM and G-AFM were considered. Here, four mostly-possible ones have been considered in DFT calculations. Furthermore, the following Monte Carlo simulation, with no bias of preset magnetic configurations, will be employed to verify the results of DFT. If there's more stable one, the Monte Carlo simulation should capture it.

The calculated electronic structure of Y-AFM with SOC are shown in 2(c-d). It is clear that $\text{Hf}_2\text{VC}_2\text{F}_2$ monolayer is a direct-gap semiconductor and the corresponding band gap is about 0.4 eV with default U_{eff} 's. The HSE06 functional calculation leads to very similar electronic structure with a larger band gap (0.9 eV).³⁸ The projection of Bloch states to V's d -orbital is also displayed in 2(c-d). As expected, there are nine occupied bands near the Fermi level mostly contributed by V's $3d$ orbitals. As expected, the d^3 configuration of V^{2+}

just occupies the t_{2g} orbitals in the half-filling manner, while the e_g orbitals are above the Fermi level. According to PDOS, there is also moderate $p-d$ hybridization, which is a bridge for superexchange interaction.

Since the Y-AFM is a type of helical spin order which breaks inversion symmetry, i.e. clockwise vs counterclockwise [3(a,b)], previous studies of triangular-lattice antiferromagnets with a helical spin order have found the magnetism induced FE P .^{27,46–48} Thus it is reasonable to expect the similar multiferroicity in the $\text{Hf}_2\text{VC}_2\text{F}_2$ monolayer.

For the Y-AFM spin order, the noncollinear spin texture forms a helical plane. It is necessary to know the easy plane/axis first. Our calculation with SOC finds that the out-of-plane c direction is the easy axis. Thus in the ground state, the helical plane should be perpendicular to the monolayer. The energy of ac (or bc) plane Y-AFM is lower than that of ab plane Y-AFM by 0.14 meV/V. Our calculation also finds the rotation symmetry within the monolayer plane. Thus the helical plane can be rotated freely along the c -axis, as sketched in 3(c).

The standard Berry phase calculation with SOC gives $1.98 \times 10^{-6} \mu\text{C}/\text{m}$ for the Y-AFM state, corresponding to $2700 \mu\text{C}/\text{m}^2$ in the 3D unit considering the thickness of monolayer 7.0 Å. To partition these two contributions, using the high-symmetric crystalline structure, the obtained pure electronic contribution (P_e) is about $1.95 \times 10^{-6} \mu\text{C}/\text{m}$, very close to the total P with ionic displacements. Therefore, here FE P is almost fully ($\sim 98.5\%$) originated from the bias of electronic cloud while the atomic structure is almost in the high symmetric one. Our calculation also indicates that the direction of P is always perpendicular to the spin helical plane, as sketched in 3(c). And this P can be switched to $-P$, once the chirality of Y-AFM is reversed. For comparison, the higher energy ab -plane Y-AFM gives $2.9 \times 10^{-7} \mu\text{C}/\text{m}$, pointing along the c -axis.

Although this P is much smaller than those of other 2D FE's, e.g. for some functionalized 2D materials ($3 \times 10^{-5} - 1.1 \times 10^{-4} \mu\text{C}/\text{m}^{15}$), 2D honeycomb binary buckled compounds ($9 \times 10^{-7} - 1.11 \times 10^{-5} \mu\text{C}/\text{m}^{13}$), and multiferroic $\text{C}_6\text{N}_8\text{H}$ organic network ($\sim 4500 \mu\text{C}/\text{m}^{24}$),

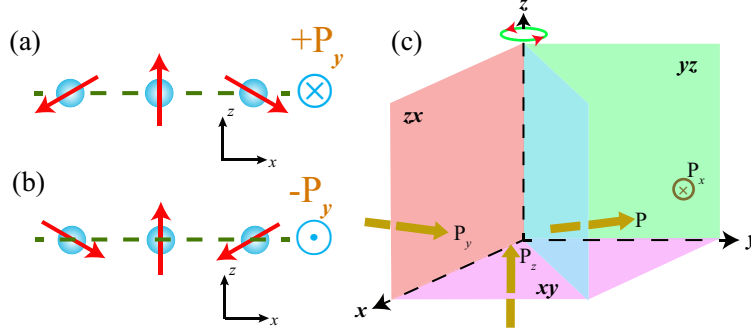


Figure 3: Schematic of helical Y-AFM induced FE \mathbf{P} . (a-b) Clockwise *vs* counter-clockwise helicity. The corresponding \mathbf{P} is perpendicular to the Y-AFM spin plane. (c) The free rotation of spin plane along the c -axis (z -axis). The higher energy ab (xy) plane is also shown. Here x - y - z forms rectangular coordinate system.

it should be noted that the origin of FE P in $\text{Hf}_2\text{VC}_2\text{F}_2$ monolayer is conceptually different from other 2D FE's. In fact, it is common sense that the improper FE P 's in the type-II multiferroics are weaker than those typical values of proper FE's.^{22,23} Even though, the origin of ferroelectricity in the type-II multiferroics guarantees the intrinsically strong magnetoelectric coupling, which is rare in other multiferroics.

In fact, $2700 \mu\text{C}/\text{m}^2$ is already a very significant value in type-II multiferroics, especially considering the fact that its origin is from the SOC, not exchange striction.^{22,23} For reference, the P in polycrystal $\text{Ba}_3\text{MnNb}_2\text{O}_9$ only reaches $3.45 \mu\text{C}/\text{m}^2$,²⁹ and $\sim 600 \mu\text{C}/\text{m}^2$ in TbMnO_3 .⁴⁹ The relatively large P is probably due to $5d$ Hf ions, which own larger SOC than $3d$ elements. Although Hf's orbitals do not contribute to magnetism directly, the hybridization between orbitals always exists around the Fermi level, which may enhance the effective SOC. Thus in principle, the macroscopic polarization should be detectable, at least in its corresponding bulk form. In addition, the second-harmonic-generation (SHG) based on nonlinear optical process can also be employed to detect the polarization and its domain without electrodes, as done for TbMnO_3 .[?] Among type-II multiferroics, some polarizations are generated by noncollinear spin order via spin-orbit coupling (SOC), as in our $\text{Hf}_2\text{VC}_2\text{F}_2$. Since SOC is usually weak especially for $3d$ electrons, the polarizations in this category are usually much smaller than those in conventional ferroelectrics.²³ Furthermore, here the high

ratio of P_e/P is also advantage for ultra-fast switching. Although it's common sense that type-II multiferroics own high P_e/P (e.g. $\sim 25\%$ in TbMnO_3 ,⁵⁰ and $\sim 58\%$ in HoMnO_3 ,⁵¹ which were estimated using the same method used here) than proper FE materials, the $P_e/P=98.5\%$ is indeed very high and rather rare.

The origin of ferroelectricity driven by helical spin order is also nontrivial. Although the spin-current model (or the Dzyaloshinskii-Moriya interaction) can explain the origin of ferroelectricity in cycloid spiral magnets,^{52,53} its equation $\mathbf{e}_{ij} \times (\mathbf{S}_i \times \mathbf{S}_j)$ gives zero net P for Y-AFM in each triangular unit. Instead, the generalized spin-current model proposed by Xiang *et al.*⁵⁴ can phenomenologically explain the origin of \mathbf{P} :

$$\mathbf{P} = \mathbf{M} \cdot \sum_{\langle ij \rangle} (\mathbf{S}_i \times \mathbf{S}_j), \quad (1)$$

where the summation is over all NN bonds; \mathbf{S} denotes a (normalized) spin vector; \mathbf{M} is a 3×3 matrix which can be determined via DFT:

$$\mathbf{M} = - \begin{bmatrix} 9.571 & 0 & 0 \\ 0 & 9.571 & 0 \\ 0 & 0 & 1.401 \end{bmatrix} \times 10^{-3} \text{e}\text{\AA}. \quad (2)$$

MC simulation. In above DFT calculations, only five magnetic candidates were considered, which could not exclude other possible exotic orders. Thus the unbiased Monte Carlo (MC) simulation is performed to verify the ground state and estimate the transition temperature.³⁸ The Heisenberg spin model is adopted:

$$H = -J_1 \sum_{\langle ij \rangle} \mathbf{S}_i \cdot \mathbf{S}_j - J_2 \sum_{[kl]} \mathbf{S}_k \cdot \mathbf{S}_l - A \sum_i (S_i^z)^2, \quad (3)$$

where J_1 (J_2) is the exchange interaction between NN (NNN) spin pairs; A is the coefficient for magnetocrystalline anisotropy and S^z is the component of spin along the magnetic easy

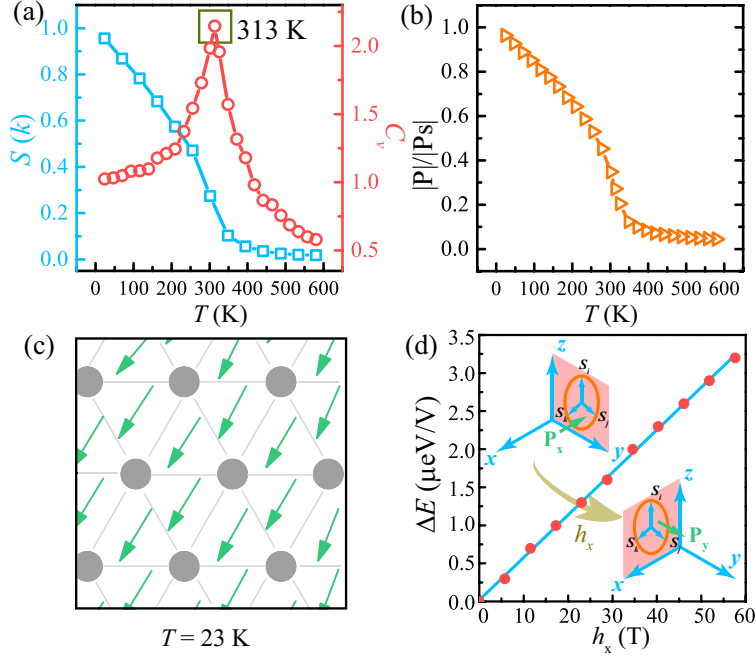


Figure 4: MC results. (a) The spin structure factor ($S(\mathbf{k}) = \sum_{ij} \langle S_i \cdot S_j \rangle e^{\mathbf{k} \cdot (r_i - r_j)}$) for Y-AFM and specific heat (C_v) as a function of temperature (T). (b) The FE $|\mathbf{P}|$ as a function of T , calculated using Eq. 1 and normalized to its saturated value $|\mathbf{P}_S|$. (c) A typical MC snapshot of \mathbf{P}_i (arrows) in a small region. Dots: V ions. (d) Energy difference between the yz plane and xz plane Y-AFM, under a magnetic field h_x along the x axis.

axis. Using the normalized $|\mathbf{S}| = 1$, these coefficients can be extracted from DFT calculations by comparing the energies of magnetic candidates:³⁸ $J_1 = -48.1$ meV, $J_2 = 6.7$ meV, and $A = 0.14$ meV, respectively. As expected, the NN exchange is strongly AFM, while the NNN is much weaker. The dominant J_1 leads to the Y-AFM, as confirmed using MC simulation [4(a)]. Interestingly, the estimated Néel temperature T_N reaches 313 K, a remarkable high T_N above room temperature. The FE $|\mathbf{P}|$ just appears below T_N [4(b)], a character of type-II multiferroicity. A typical MC snapshot of local \mathbf{P}_i 's (of V triangular units) at low temperature is shown in 4(c).

For most 3D type-II multiferroics, the magnetism and ferroelectricity only appear far below room temperature.²³ High-temperature type-II multiferroicity is a highly desired property for applications, which is a bottleneck for this category of materials. Till now, in various type-II multiferroics, only a few hexagonal ferrites with very complex crystalline/magnetic structures show magnetoelectricity above room temperature.⁵⁵ $\text{Hf}_2\text{VC}_2\text{F}_2$ is another room-temperature type-II multiferroic system, with a much simpler crystalline/magnetic structure.

Physically, its high T_N is due to the ideal half-filled t_{2g} orbitals ($3d^3$), which prefers a strong superexchange according to the Goodenough-Kanamori rule.^{41,42} The similar case is for various ferrites with Fe^{3+} ($3d^5$) ions, which usually own magnetic orders above room temperature.

As a type-II multiferroic, the induced \mathbf{P} can be fully controlled by magnetic fields via the helical plane rotation.³⁸ As shown in 4(d), under an in-plane magnetic field, the energies of yz -plane and xz -plane Y-AFM (after slight distortions driven by magnetic field) are no longer degenerated. Thus, the helical plane of Y-AFM and its associated \mathbf{P} should rotate accompanying the field. Since there's no intrinsic energy barrier for such a helical plane rotation, this magnetoelectric response should work under small fields.

Last, the MoSe_2 substrate is considered to test the possible substrate effect.³⁸ With proximate in-plane lattice constants, the optimized distance between $\text{Hf}_2\text{VC}_2\text{F}_2$ monolayer and MoSe_2 substrate is ~ 3.5 Å, indicating the vdW interaction. No charge transfer occurs be-

tween $\text{Hf}_2\text{VC}_2\text{F}_2$ and substrate. The Y-AFM remains the ground state, and the whole system remains insulating. Therefore, the substrate will not change the conclusion of multiferroicity for $\text{Hf}_2\text{VC}_2\text{F}_2$ monolayer.

Conclusion. The noncollinear 120° Y-type antiferromagnetic order is predicted to be the ground state in MXene $\text{Hf}_2\text{VC}_2\text{F}_2$ monolayer, and the estimated Néel point can be above room temperature. More importantly, the inversion symmetry is broken by this particular Y-type antiferromagnetic order, resulting in the improper magnetism-driven ferroelectric polarization. Thus $\text{Hf}_2\text{VC}_2\text{F}_2$ monolayer is a room-temperature type-II multiferroics, which has intrinsically strong magnetoelectric coupling. The crossover between 2D materials and magnetic ferroelectrics will be a very interesting topic, both fundamentally and to benefit nanoscale devices.

Acknowledgement

Work was supported by National Natural Science Foundation of China (Grant No. 11674055), Fundamental Research Funds for the Central Universities, Jiangsu Innovation Projects for Graduate Student (Grant No. KYLX16_0116), and National Supercomputer Center in Guangzhou (NSCC-GZ).

References

- (1) Novoselov, K. S.; Geim, A. K.; Morozov, S.; Jiang, D.; Zhang, Y.; Dubonos, S. V.; Grigorieva, I. V.; Firsov, A. A. *Science* **2004**, *306*, 666–669.
- (2) Ge, J.-F.; Liu, Z.-L.; Liu, C.; Gao, C.-L.; Qian, D.; Xue, Q.-K.; Liu, Y.; Jia, J.-F. *Nat. Mater.* **2015**, *14*, 285–289.
- (3) Zhang, J.-J.; Gao, B.; Dong, S. *Phys. Rev. B* **2016**, *93*, 155430.
- (4) Zhang, J.-J.; Dong, S. *2D Mater.* **2016**, *3*, 035006.

- (5) Zhang, J.-J.; Dong, S. *J. Chem. Phys.* **2017**, *146*, 034705.
- (6) Lei, J.; Kutana, A.; Yakobson, B. I. *J. Mater. Chem. C* **2017**, *5*, 3438–3444.
- (7) Huang, B.; Clark, G.; Navarro-Moratalla, E.; Klein, D. R.; Cheng, R.; Seyler, K. L.; Zhong, D.; Schmidgall, E.; McGuire, M. A.; Cobden, D. H.; Yao, W.; Xiao, D.; Jarillo-Herrero, P.; Xu, X. D. *Nature* **2017**, *546*, 270–273.
- (8) Dong, L.; Kumar, H.; Anasori, B.; Gogotsi, Y.; Shenoy, V. B. *J. Phys. Chem. Lett.* **2017**, *8*, 422–428.
- (9) Yang, J. H.; Zhou, X. M.; Luo, X. P.; Zhang, S. Z.; Chen, L. *Appl. Phys. Lett.* **2016**, *109*, 203109.
- (10) Wu, M.; Burton, J. D.; Tsymbal, E. Y.; Zeng, X. C.; Jena, P. *Phys. Rev. B* **2013**, *87*, 081406.
- (11) Kan, E.; Wu, F.; Deng, K. M.; Tang, W. H. *Appl. Phys. Lett.* **2013**, *103*, 193103.
- (12) Shirodkar, S. N.; Waghmare, U. V. *Phys. Rev. Lett.* **2014**, *112*, 157601.
- (13) Di Sante, D.; Stroppa, A.; Barone, P.; Whangbo, M.-H.; Picozzi, S. *Phys. Rev. B* **2015**, *91*, 161401.
- (14) Ding, W. J.; Zhu, J. B.; Wang, Z.; Gao, Y. F.; Xiao, D.; Gu, Y.; Zhang, Z. Y.; Zhu, W. G. *Nat. Commun.* **2017**, *8*, 14956.
- (15) Wu, M.; Dong, S.; Yao, K. L.; Liu, J. M.; Zeng, X. C. *Nano Lett.* **2016**, *16*, 7309–7315.
- (16) Wu, M.; Zeng, X. C. *Nano Lett.* **2016**, *16*, 3236–3241.
- (17) Chandrasekaran, A.; Mishra, A.; Singh, A. K. *Nano Lett.* **2017**, *17*, 3290–3296.
- (18) Fei, R. X.; Kang, W.; Yang, L. *Phys. Rev. Lett.* **2016**, *117*, 097601.
- (19) Li, L.; Wu, M. *ACS Nano* **2017**, *11*, 6382–6388.

- (20) Chang, K.; Liu, J. W.; Lin, H. C.; Wang, N.; Zhao, K.; Zhang, A. M.; Jin, F.; Zhong, Y.; Hu, X. P.; Duan, W. H.; Zhang, Q. M.; Fu, L.; Xue, Q.-K.; Chen, X.; Ji, S.-H. *Science* **2016**, *353*, 274–278.
- (21) Liu, F. et al. *Nat. Commun.* **2016**, *7*, 12357.
- (22) Cheong, S.-W.; Mostovoy, M. *Nat. Mater.* **2007**, *6*, 13.
- (23) Dong, S.; Liu, J.-M.; Cheong, S.-W.; Ren, Z. F. *Adv. Phys.* **2015**, *64*, 519–626.
- (24) Tu, Z. Y.; Wu, M.; Zeng, X. C. *J. Phys. Chem. Lett.* **2017**, *8*, 1973–1978.
- (25) Yang, Q.; Xiong, W.; Zhu, L.; Gao, G. Y.; Wu, M. *J. Am. Chem. Soc.* **2017**, *139*, 11506–11512.
- (26) Khomskii, D. *Physics* **2009**, *2*, 20.
- (27) Kimura, T.; Lashley, J.; Ramirez, A. *Phys. Rev. B* **2006**, *73*, 220401.
- (28) Liu, M. F.; Zhang, H. M.; Huang, X.; Ma, C. Y.; Dong, S.; Liu, J.-M. *Inorg. Chem.* **2016**, *55*, 2709–2716.
- (29) Lee, M.; Choi, E. S.; Huang, X.; Ma, J.; Delacruz, C. R.; Matsuda, M.; Tian, W.; Dun, Z. L.; Dong, S.; Zhou, H. D. *Phys. Rev. B* **2014**, *90*, 224402.
- (30) Naguib, M.; Kurtoglu, M.; Presser, V.; Lu, J.; Niu, J. J.; Heon, M.; Hultman, L.; Gogotsi, Y.; Barsoum, M. W. *Adv. Mater.* **2011**, *23*, 4248–4253.
- (31) Naguib, M.; Mashtalir, O.; Carle, J.; Presser, V.; Lu, J.; Hultman, L.; Gogotsi, Y.; Barsoum, M. W. *ACS Nano* **2012**, *6*, 1322–1331.
- (32) Naguib, M.; Halim, J.; Lu, J.; Cook, K. M.; Hultman, L.; Gogotsi, Y.; Barsoum, M. W. *J. Am. Chem. Soc.* **2013**, *135*, 15966–15969.

- (33) Khazaei, M.; Arai, M.; Sasaki, T.; Chung, C.-Y.; Venkataramanan, N. S.; Estili, M.; Sakka, Y.; Kawazoe, Y. *Adv. Funct. Mater.* **2013**, *23*, 2185–2192.
- (34) Liu, Z.; Zheng, L.; Sun, L.; Qian, Y.; Wang, J.; Li, M. *J. Am. Ceram. Soc.* **2014**, *97*, 67–69.
- (35) Anasori, B.; Halim, J.; Lu, J.; Voigt, C. A.; Hultman, L.; Barsoum, M. W. *Scr. Mater.* **2015**, *101*, 5–7.
- (36) Anasori, B.; Xie, Y.; Beidaghi, M.; Lu, J.; Hosler, B. C.; Hultman, L.; Kent, P. R.; Gogotsi, Y.; Barsoum, M. W. *ACS Nano* **2015**, *9*, 9507–9516.
- (37) Zhou, J.; Zha, X. H.; Zhou, X. B.; Chen, F. Y.; Gao, G. L.; Wang, S. W.; Shen, C.; Chen, T.; Zhi, C. Y.; Eklund, P.; Du, S. Y.; Xue, J. M.; Shi, W. Q.; Chai, Z. F.; Huang, Q. *ACS Nano* **2017**, *11*, 3841–3850.
- (38) See Supplemental Materials for details of DFT and MC methods, as well as more results of $\text{Hf}_2\text{VC}_2\text{F}_2$ and other $\text{Hf}_2\text{MC}_2\text{X}_2$.
- (39) Ratcliff, W.; Lynn, J. W.; Kiryukhin, V.; Jain, P.; Fitzsimmons, M. R. *NPJ Quant. Mater.* **2016**, *1*, 16003.
- (40) Lin, L.; Zhang, H. M.; Liu, M. F.; Shen, S. D.; Zhou, S.; Li, D.; Wang, X.; Yan, Z. B.; Zhang, Z. D.; Zhao, J.; Dong, S.; Liu, J.-M. *Phys. Rev. B* **2016**, *93*, 075146.
- (41) Goodenough, J. B. *J. Phys. Chem. Solids* **1958**, *6*, 287–297.
- (42) Kanamori, J. *J. Phys. Chem. Solids* **1959**, *10*, 87–98.
- (43) Lapauw, T.; Tunca, B.; Cabioch, T.; Lu, J.; Persson, P. O.; Lambrinou, K.; Vleugels, J. *Inorg. Chem.* **2016**, *55*, 10922–10927.
- (44) Khazaei, M.; Arai, M.; Sasaki, T.; Estili, M.; Sakka, Y. *Science and technology of advanced materials* **2014**, *15*, 014208.

- (45) Gou, G.; Grinberg, I.; Rappe, A. M.; Rondinelli, J. M. *Phys. Rev. B* **2011**, *84*, 144101.
- (46) Seki, S.; Yamasaki, Y.; Shiomi, Y.; Iguchi, S.; Onose, Y.; Tokura, Y. *Phys. Rev. B* **2007**, *75*, 100403.
- (47) Singh, K.; Maignan, A.; Martin, C.; Simon, C. *Chem. Mater.* **2009**, *21*, 5007–5009.
- (48) Xiang, H. J.; Kan, E. J.; Zhang, Y.; Whangbo, M. H.; Gong, X. *Phys. Rev. Lett.* **2011**, *107*, 157202.
- (49) Kimura, T.; Goto, T.; Shintani, H.; Ishizaka, K.; Arima, T.; Tokura, Y. *Nature (London)* **2003**, *426*, 55–58.
- (50) Walker, H. C.; Fabrizi, F.; Paolasini, L.; de Bergevin, F.; Herrero-Martin, J.; Boothroyd, A. T.; Prabhakaran, D.; McMorrow, D. F. *Science* **2011**, *333*, 1273–1276.
- (51) Picozzi, S.; Yamauchi, K.; Sanyal, B.; Sergienko, I. A.; Dagotto, E. *Phys. Rev. Lett.* **2007**, *99*, 227201.
- (52) Katsura, H.; Nagaosa, N.; Balatsky, A. V. *Phys. Rev. Lett.* **2005**, *95*, 057205.
- (53) Sergienko, I. A.; Dagotto, E. *Phys. Rev. B* **2006**, *73*, 094434.
- (54) Xiang, H. J.; Kan, E. J.; Zhang, Y.; Whangbo, M.-H.; Gong, X. G. *Phys. Rev. Lett.* **2011**, *107*, 157202.
- (55) Kimura, T. *Annu. Rev. Condens. Matter Phys.* **2012**, *3*, 93–110.